Electronic Supplementary Material (ESI) for Journal of Materials Chemistry C.

Supporting Information

Novel insights in the magnetic behaviour of non-stoichiometric $LaMnO_{3+\delta}$ nanoparticles

Raquel Cortés-Gil,[a] Antonio Hernando,[b,c,d] José M. Alonso,[b,e] Kevin M. Sigcho,[a] Alberto Azor-Lafarga,[a] José L. Martínez,[e] M. Luisa Ruiz-González[a]* and José M. González-Calbet[a,f]*

[a] Departamento de Química Inorgánica, Facultad de Químicas, Universidad Complutense, CEI Moncloa, 28040 Madrid, Spain Email: jgcalbet@ucm.es Email: luisarg@ucm.es

[b] Instituto de Magnetismo Aplicado, UCM-CSIC-ADIF, P.O. Box 155, 28230 Las Rozas de Madrid, Spain

[c] IMDEA Nanociencia, Faraday 9, 28049 Madrid, Spain.

[d] Donostia International Physics Centre, Manuel Lardizabal, Ibilbidea 4, 20018 San Sebastian, Guipuzkoa, Spain.

[e] Instituto de Ciencia de Materiales, CSIC, Sor Juana Inés de la Cruz s/n, 28049 Madrid, Spain

[f] ICTS Centro Nacional de Microscopia Electrónica-ELECMI, Universidad Complutense, CEI Moncloa 28040-Madrid, Spain

S1. X Ray Diffraction and Low Magnification TEM

The XRD patterns for $La_{0.93}Mn_{0.93}O_3$ and $LaMnO_3$ can be indexed on the basis of a rhombohedral perovskite unit cell (SG $R\bar{3}c$) as observed in the final refinement of the XRD patterns (Figure S1). The lattice parameters for both samples, together with the final structural parameters are gathered in Tables S1.1 and S1.2. It is worth recalling, that the bulk systems, $LaMnO_{3+\delta}$[1,2] and $LaMnO_3$,[3] exhibit rhombohedral and orthorhombic symmetries, respectively. According to Debye Scherrer equation, the average crystallite size is around 30 nm for both compositions. The results agree with TEM data from which the average particle size is around 25 nm (insets of Figure 1-b). According to reference 4, we have carried out fittings of the histograms with different distribution functions: Gaussian, Lorentzian and LogNormal. All of them lead to the same particle size: around 24 nm. Nevertheless, the best correlation taking into account the same criteria for both samples corresponds to the LogNormal distribution function: average particle size (D) of 24.08 ± 0.03 nm and 24.02 ± 0.04 nm for $LaMnO_3$ and $La_{0.93}Mn_{0.93}O_3$, respectively with determination coefficient (R^2) of 0.97609 and 0.96808, for $LaMnO_3$ and $La_{0.93}Mn_{0.93}O_3$, respectively.

Figure S1

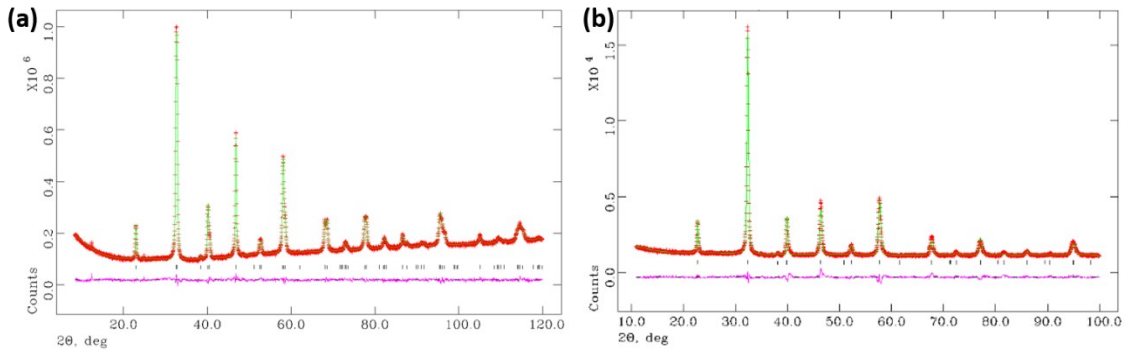

(a, b). XRD pattern (red points) and Rietveld fit (green line) of $La_{0.93}Mn_{0.93}O_3$ and $LaMnO_3$ NPs, respectively, at room temperature. The difference between experimental and calculated data is shown as a solid line below. Vertical bars show all allowed reflections of the SG $R\bar{3}c$.

Table S1.1. Structural parameters for $La_{0.93}Mn_{0.93}O_3$ NPs from the Rietveld refinement of the XRD pattern at 300 K.

Atom	Site	x	Y	z	10^4 x Uiso (Å^2)
La	6*a*	0	0	0.25	32.7(1)
Mn	6*b*	0	0	0	29.8(1)
O	18*e*	0.4579(2)	0	0.25	32.1(1)

Space group $R\bar{3}c$. Lattice parameters a=0.55124(1) and c=1.33696(5) nm. R_{wp}=0.0230, R_p=0.0181, χ^2=1.508, 38 variables.

Table S1.2. Structural parameters for $LaMnO_{3.00}$ NPs from the Rietveld refinement of the XRD pattern at 300 K.

Atom	**Site**	**x**	**Y**	**z**	**10^4 x Uiso (Å^2)**
La	6*a*	0	0	0.25	50.5(1)
Mn	6*b*	0	0	0	8.36(1)
O	18*e*	0.4410(3)	0	0.25	38.4(1)

Space group $R\bar{3}c$. Lattice parameters a=0.55306(4) and c=1.35527(5) nm. R_{wp}=0.0250, R_p=0.0183, χ^2=2.369, 38 variables.

S2. Average cationic composition

Table S2.1 Average cationic composition by means of EPMA corresponding to $La_{0.93}Mn_{0.93}O_3$ and $LaMnO_3$ NPs in 10 areas of around 200 μm.

	Mn	**La**	**La/Mn (±0.10)**	**Composition**
$La_{0.93}Mn_{0.93}O_3$	49.5	51.0	1.03	$La_{1.03}Mn_{0.97}$
$LaMnO_3$	49.8	50.2	1.01	$La_{1.01}Mn_{0.99}$

Figure S2

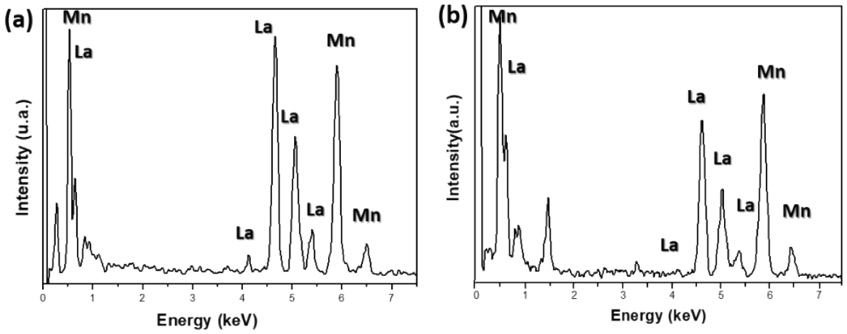

Characteristic EDS spectrum of (a) $La_{0.93}MnO_{0.93}O_3$ and (b) $LaMnO_3$ NPs.

S3. Thermogravimetric analysis

The oxidized NPs were heated in an H_2 (200 mbar) and He (300 mbar) atmosphere until 900 °C at 6 °C/min ratio in a Cahn D-200 electrobalance. The XRD analysis of the total reduction products led to a mixture of La_2O_3 and MnO. Under these conditions, the reduction process takes place in four stages (figure 1c).

According to previous results, the first one (25≤T≤310 °C) must correspond to the desorption of adsorbed water and other impurities (NO_x) on the NPs. On the basis of this result, the weight loss since the beginning of the stage II, taking also into account the cationic stoichiometry data, indicates the stabilization of a sample with the general formula $LaMnO_{3.23}$, involving 45 % Mn^{4+}. However, as was discussed in the introduction section, the perovskite structure does not admit interstitial oxygen and instead of that the system develops onto the Mn and La vacancy formation. As a consequence, cation vacancies are created in accordance to the $La_{1-t}Mn_{1-t}O_3$ formula and a $La_{0.93}Mn_{0.93}O_3$ composition must be considered. In this sense, stage II (310≤T≤450 °C) corresponds to the reduction of the oxidized material, with 45 % Mn^{4+}, up to the stoichiometric $LaMnO_3$. The stage III (450≤T≤670 °C) corresponds to the reduction of stoichiometric $LaMnO_3$ to $LaMnO_{2.88}$.[5] The last stage (670≤T≤780 °C) corresponds to the final decomposition of $LaMnO_{2.88}$ giving rise to La_2O_3 and MnO.

$LaMnO_3$ NPs were obtained by topotactic reduction of $La_{0.93}Mn_{0.93}O_3$ in the electrobalance at 350 °C. Taking into account the above considerations, we therefore proceeded to make a cleaning pretreatment of the sample which consists in reproduce the synthesis conditions heating the sample in air until 650 °C. Once the oxygen mass corresponding to the stage I was removed (H_2O and NO_x with a loss weigh of 1.74 %), the reduction process started from room temperature at 0.1 °C/min until an additional weight loss of 1.50 % was achieved, corresponding to the leads to the stabilization of $LaMnO_3$ NPs at 350 °C. At this temperature, the reducing atmosphere was replaced by an inert one, 500 mbar of He, and the sample was quenched to room temperature. A small portion of this sample was totally reduced in the electrobalance in order to assure an oxygen content corresponding to 3.0 per unit formula.

S4. ABF (annular bright-field) images

In ABF imaging, the collection angle is modified (11-22 mrad) to enhance the contrast of the lighter elements. The required system in the JEOL-JEM ARM200 microscope consists on a bright field detector in which the central area is blanked with a beam stopper providing an annular detector. By modifying the camera length, the appropriate solid angle to enhance the contrast of the oxygen atomic columns is optimized. The resulting image allows the visualization of both light and heavy atomic columns. Acquisition times of 38 s per frame were used for HAADF and ABF images. Figure S4 shows HAADF and ABF images simultaneously acquired of a characteristic $La_{0.93}Mn_{0.93}O_3$ NPs. Both cationic and anionic sublattices are visualized.

Figure S4

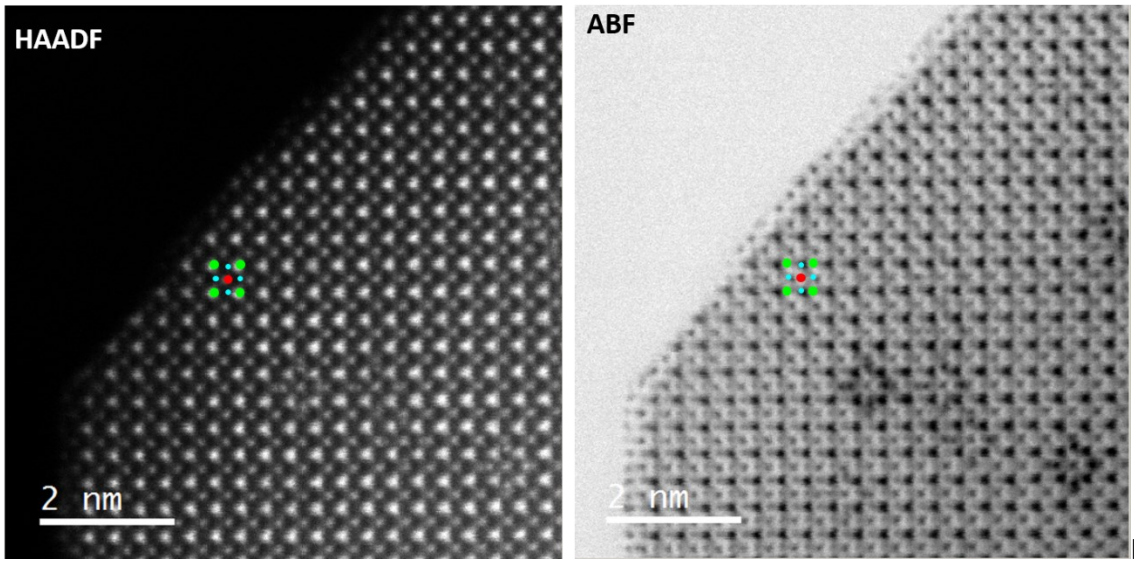

HAADF and ABF images simultaneously acquired. The oxygen sublattice is visible according to the perovskite lattice in the ABF images where the atoms columns are seen in gray scale. Schematic ball model unit cell has been inserted (Green: La; Red: Mn; Blue: O).

S5. STEM-HAADF simulation of the additional La columns

In order to provide complementary information to the experimental visualization of additional columns of La, we have performed an image calculation of the defective cell under the basis of the cubic subcell

taking into account the extra atomic coordinates depicted in table S5.1. The occupancy for La atoms has been fixed to 0.46, i.e. half of 0.93, based on the experimental fact that the intensity of the normal La sites surrounding the defects is lower than the one corresponding to the normal La columns far from them, but similarly to the interstitial La columns. The x and y coordinates have been extracted from the HAADF image shown in figure 2b. The z coordinate is fixed to 0.5. The resulting cell according to this model is shown in figure S5.1. The image simulation has been performed using the multislice method with the MacTempas software (6). The parameters used in this simulation are gathered in table S5.2. The simulated images for different thickness are shown in figure S5.2.

Table S5.1 Atomic positions for the extra La atoms in the cubic perovskite subcell.

Atom	x	y	z
La1	0.5	0.125	0.5
La2	0.5	0.875	0.5
La3	0.125	0.5	0.5
La4	0.875	0.5	0.5

Figure S5.1

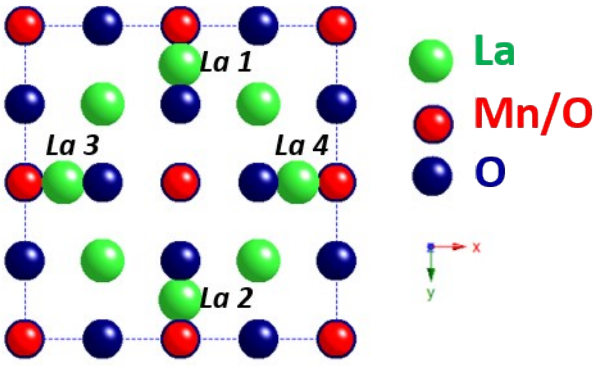

Schematic structural model along [001] corresponding to the defects observed in figure 2b, derived from the cubic subcell and the additional coordinates of table S5.1.

Table S5.2 Simulation parameters

Voltage (kV)	120 kV
Probe sampling	0.08 Å/px
Sampling points	400
Convergence angle	30 mrad
Spherical aberration coefficient (C3)	5μm
Inner aperture	90 mrad
Outer aperture	300 mrad

Figure S5.2

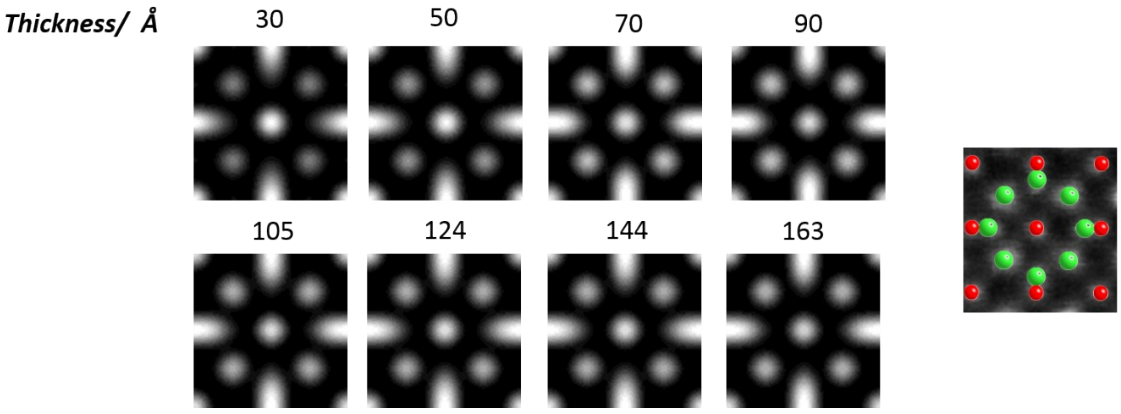

Calculated images from different thickness. The experimental unit cell with the overlapping La and Mn sites according to the model.

S6. Electron Energy Loss Spectroscopy

In addition to the EELS information displayed in the main text, the Mn^{3+}/Mn^{4+} ratio has been estimated by analyzing the relative intensity of the Mn-L_2 and Mn-L_3 white lines from the fitting of the second derivative of the Mn-$L_{2,3}$ white lines to a Gaussian curve (Table S6.1) using the Gatan GMS2 software.

Table S6.1 Intensity I(L_3/L_2) ratio for $La_{0.93}Mn_{0.93}O_3$, $LaMnO_3$ NPs and references for Mn^{4+} ($CaMnO_3$), Mn^{3+} ($LaMnO_3$) and Mn^{2+} ($CaMnO_2$).

Sample	**I (L_3/L_2)**
$CaMnO_3$ (Mn^{4+})	1.8 (±0.1)
$LaMnO_3$ (Mn^{3+})	2.4 (±0.1)
$CaMnO_2$ (Mn^{2+})	5.5 (±0.1)
$La_{0.93}Mn_{0.93}O_3$ NPs	2.25 (±0.1)
$LaMnO_3$ NPs	2.4 (±0.1)

S7. MAGNETISM

Figure S7.

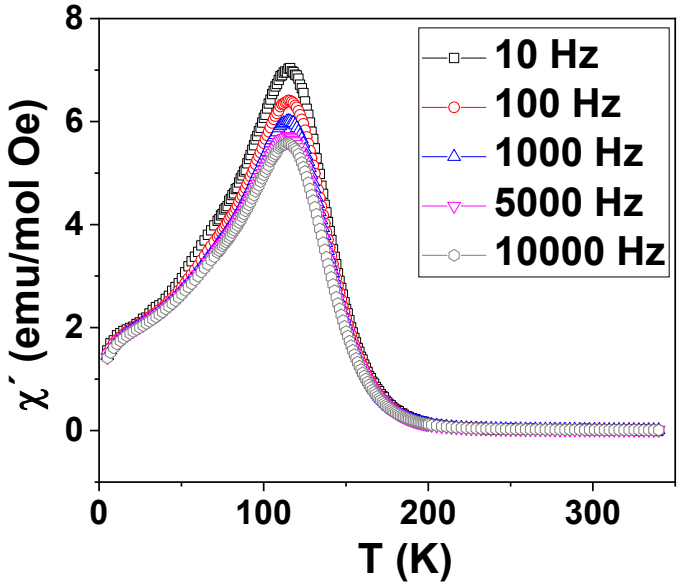

Temperature dependence of real part of AC magnetic susceptibility of $LaMnO_3$ NPs under 1 Oe oscillating magnetic field and a frequency range from 10 to 10000 Hz.

References

(1) Q. Huang, A. Santoro, J. W. Lynn, R. W. Erwin, J. A. Borchers, J. L. Peng. R. L. Greene, Structure and magnetic order in undoped lanthanum manganite, *Phys. Rev*. B, 1997, **55**, 14987-14999.

(2) C. Ritter, M.R. Ibarra, J. M. de Teresa, P. A. Algarabel, C. Marquina, J. Blasco, J. García, S. Oseroff, S-W. Cheong, Influence of oxygen content on the structural, magnetotransport, and magnetic properties of $LaMnO_{3+\delta}$, *Phys. Rev*. B 1997, **56**, 8902-8911.

(3) J. Rodríguez-Carvajal, M. Hennion, F. Moussa, A. H. Moudden, L. Pinsard, A. Revcolevschi, Neutron-diffraction study of the Jahn-Teller transition in stoichiometric $LaMnO_3$, *Phys. Rev*. B, 1998, **57(6)**, R3189-3192.

(4) Z. Wei, A. V. Pashchenko, N. A. Liedienov, I. V. Zatovsky, D. S. Butenko, Q. Li, I. V. Fesych, V. A. Turchenko, E. E. Zubov, P. Yu. Polynchuk, V. G. Pogrebnyak, V. M. Poroshini, G. G. Levchenko, Multifunctionality of lanthanum–strontium manganite nanopowder, *Phys. Chem. Chem. Phys.*, **2020**, 22, 11817-11828.

(5) R. Cortés-Gil, A. Arroyo, L. Ruiz-González, J. M. Alonso, A. Hernando, J. M. González-Calbet, M. Vallet-Regí. Evolution of magnetic behaviour in oxygen deficient $LaMnO_{3-\delta}$. *J. Phys. Chem. Solids* **2006**, *67*, 579–582.

(6) M. A. O´Keefe, R. Kilaas. Scanning Microscopy Suppl. **1988**, 225-244